ACS OMEGA

http://pubs.acs.org/journal/acsodf

Article

Crystal Forms of the Antihypertensive Drug Irbesartan: A Crystallographic, Spectroscopic, and Hirshfeld Surface Analysis Investigation

Andrea Mariela Araya-Sibaja,* Cinira Fandaruff, Ana María Guevara-Camargo, Felipe Vargas-Huertas, William J. Zamora, José Roberto Vega-Baudrit, Teodolito Guillén-Girón, Mirtha Navarro-Hoyos, Paola Paoli, Patrizia Rossi, and William Jones

Cite This: *ACS Omega* 2022, 7, 14897−14909

Read Online

ACCESS | Metrics & More | Article Recommendations

ABSTRACT: The design of new pharmaceutical solids with improved physical and chemical properties can be reached through in-detail knowledge of the noncovalent intermolecular interactions between the molecules in the context of crystal packing. Although crystallization from solutions is well-known for obtaining new solids, the effect of some variables on crystallization is not yet thoroughly understood. Among these variables, solvents are noteworthy. In this context, the present study aimed to investigate the effect of ethanol (EtOH), acetonitrile (MeCN), and acetone (ACTN) on obtaining irbesartan (IBS) crystal forms with 2,3-dibromosuccinic acid. Crystal structures were solved by single-crystal diffraction, and the intermolecular interactions were analyzed using the Hirshfeld surfaces analysis. The characterization of physicochemical properties was carried out by powder X-ray diffraction, Fourier transform infrared spectroscopy (FT-IR), thermal analysis, and solution-state NMR techniques. Two different IBS salts were obtained, one from MeCN and ACTN (compound **1**) and a different one from EtOH (compound **2**). The experimental results were in agreement with the findings obtained through quantum mechanics continuum solvation models. Compound **1** crystallized as a monoclinic system $P2_1/c$, whereas compound **2** in a triclinic system $P\bar{1}$. In both structures, a net of strong hydrogen bonds is present, and their existence was confirmed by the FT-IR results. In addition, the IBS cation acts as a H-bond donor through the N1 and N6 nitrogen atoms which interact with the bromide anion and the water molecule O1W in compound **1**. Meanwhile, N1 and N6 nitrogen atoms interact with the oxygen atoms provided by two symmetry-related 2,3-dibromo succinate anions in compound **2**. Solution-state NMR data agreed with the protonation of the imidazolone ring in the crystal structure of compound 1. Both salts presented a different thermal behavior not only in melting temperature but also in thermal stability.

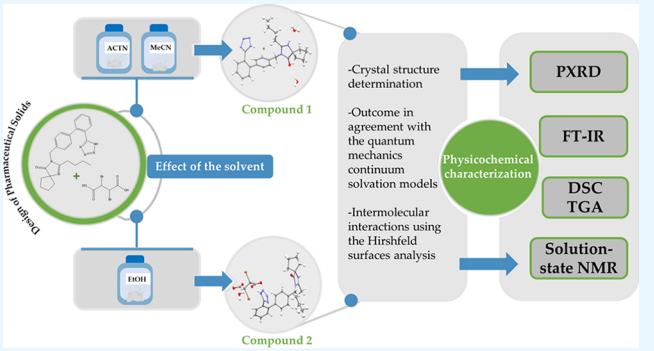

INTRODUCTION

The crystallization process to obtain different crystal forms has been extensively explored as a strategy to improve the limited bioavailability imposed by poorly water-soluble drugs.[1−4] Although the influence of the process on the properties of dosage forms and products is well-documented, however, the effects of some variables are not well-understood.[5−7] In this scenario, it is noteworthy that the crystallization process has evolved from an empirical to a theory-based science and has allowed the launching of safer products.[8] Furthermore, this knowledge has been applied to controlling the factors that impact phase transformations in the solid-state.[9,10] Therefore, the effects of crystallization variables need to be thoroughly investigated for each drug, specifically by experimental methods.

Solvents are one of those variables that have a considerable impact on the crystallization products[9,11,12] because the solute−solvent interactions are responsible for changing the molecular packing to form a different polymorph. Moreover, solvents can easily enter the crystal lattice to form solvated compounds.[9,13−15] Regarding the diversity of solvents used in the crystallization process, not only the solvent itself but also the volume of the solvent added influences the polymorphic

Received: January 26, 2022
Accepted: March 30, 2022
Published: April 19, 2022

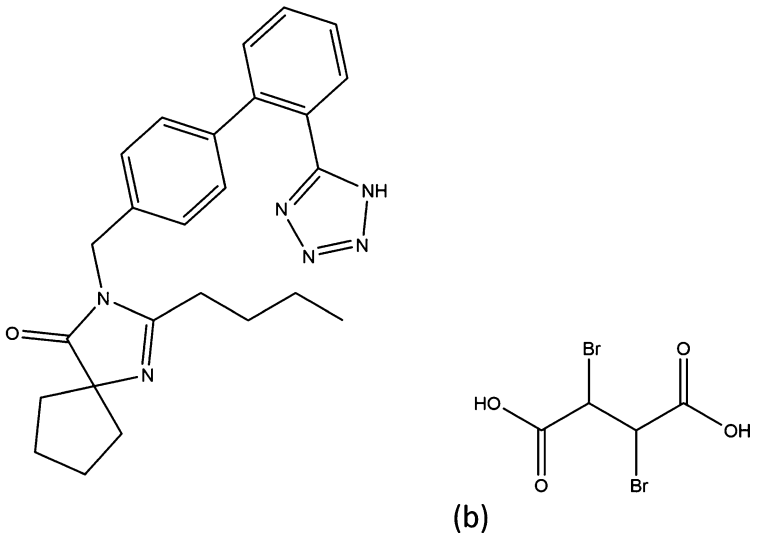

Figure 1. Chemical structure of (a) IBS and (b) DBS.

outcome, as demonstrated by Hasa and co-workers during the liquid-assisted mechanochemical reactions.[16]

Irbesartan (IBS), a poorly water-soluble drug used in the treatment of hypertension,[17] exhibits desmotropy, the property of tautomers to crystallize as two different crystal structures. Recently, the effect of solvent polarity on the selectively obtained form A and form B has been investigated,[18] as well as one cationic salt and one anionic salt of IBS were successfully obtained.[19] These characteristics indicate IBS as a potentially highly diverse and numerous solid forms system. Therefore, the interest of this study is to investigate the influence of the solvent on obtaining different IBS crystal forms, both experimentally and supported by a theory-based study. To achieve this goal, the crystallization experiment of IBS along with a molecule containing a highly electronegative element (Figure 1) 2,3-dibromosuccinic acid (DBS), which is a pharmaceutical intermediate, from three solvents was conducted. The crystal structure of the solid forms obtained was determined via single-crystal X-ray diffraction (XRD), and the intermolecular interactions in the solid-state were analyzed using the Hirshfeld surfaces (HSs) analysis. The bulk material was prepared for a deep characterization, including powder XRD (PXRD), Fourier transform infrared spectroscopy (FT-IR), thermal analysis, and solution-state NMR techniques. Furthermore, the solvent effect was studied through quantum mechanics continuum solvation models.

EXPERIMENTAL SECTION

IBS, in its crystalline form A, was kindly donated by CALOX de Costa Rica and was further characterized[20] before the crystallization experiments; DBS (purity ≥ 98%) and HPLC/UV-grade solvents were purchased from Sigma-Aldrich (purity ≥ 99.9%).

Crystallization Experiments. To obtain good quality crystals of $([C_{25}H_{29}N_6O]^+Br^-)\cdot 1{,}5(H_2O)$ (**1**) and $([C_{25}H_{29}N_6O]_2^+(C_4H_2O_4Br_2)^-)\cdot 2(H_2O)$ (**2**) 140 mg of IBS, 60 mg of DBS, and 1.5 mL of each individual solvent, ethanol (EtOH), acetone (ACTN), and acetonitrile (MeCN), were placed in a 10 mL glass vials. The mixture was heated to 70 °C while being magnetically stirred for around 10 min until it reached a clear solution. The solution was left to cool down to room temperature then the vials were sealed and stored. Nearly 5 days later, suitable crystals for structure determination were grown and withdrawn from the solution. The crystal structure obtained from ACTN and MeCN crystallizations corresponded to the same compound named **1**, whereas the one obtained from EtOH exhibited a different crystal structure identified as compound **2**.

Bulk material for further characterization was obtained using the same procedure described above, scaling up 10-fold. The crystals were collected from the solution, dried at ambient conditions, and ground to obtain a homogeneous powder. Then, the powdered material was analyzed through PXRD and compared with the calculated patterns of the structures obtained via single-crystal XRD.

X-ray Data Collection and Crystal Structure Resolution. Intensity data for compound **1** (crystallized both from ACTN and MeCN) and for compound **2** (crystallized from EtOH) were collected at 100 K by using a Bruker Apex-II CCD diffractometer. The program used for the data collection was Bruker APEX2.[21] While they were integrated and reduced by the Bruker SAINT software,[22] absorption correction was performed with SADABS-2016/2.[23] The radiation used were Mo Kα (λ = 0.71073 Å) and Cu Kα (λ = 1.54184 Å) for **1** and **2**, respectively.

Crystal structures were solved using the SHELXS-97 program[24] and refined by full-matrix least-squares against F^2 using all data (SHELXL-2018/3[25]).

All nonhydrogen atoms were refined with anisotropic displacement parameters; the hydrogen atoms bonded to N1 and N6 in the two structures, as well as the water hydrogen atoms, were found in the Fourier density map. Their coordinates were freely refined while their thermal parameters were set in accordance with one of the atoms to which they are bonded. All the other hydrogen atoms were introduced in a calculated position. The final carbon atoms, C10 and C11, of the *n*-butyl chain in **1** are in a disordered position; such disorder was modeled by introducing two models for each atom (occupancy factors were set at 0.7 and 0.3 for models A and B, respectively). Finally, one of the two water molecules in **1** (the one with the oxygen atom labeled O2W) has an occupancy factor of 0.5.

https://doi.org/10.1021/acsomega.2c00545
ACS Omega 2022, 7, 14897−14909

Table 1. Crystallographic Data and Refinement Parameters for 1 and 2 Crystals

	1	2
formula	$([C_{25}H_{29}N_6O]Br)\cdot 1{,}5(H_2O)$	$([C_{25}H_{29}N_6O]_2(C_4H_2O_4Br_2))\cdot 2(H_2O)$
M	536.47	1168.98
T (K)	273	273
λ (Å)	0.71073	1.54184
crystal system, space group	monoclinic, $P2_1/c$	triclinic, $P\bar{1}$
unit cell dimensions (Å, deg)	a = 12.516(2) b = 24.969(5); β = 104.865(4) b = 11.857(2); β = 100.835(5) c = 8.432(1) c = 12.552(2); γ = 90.184(5)	a = 9.515(1); α = 91.553(5)
V (Å^3)	2546.8(8)	1345.3(3)
Z, d (g/cm^3)	4, 1.399	1, 1.443
μ (mm^{-1})	1.650	2.453
F(000)	1116	606
2θ range (deg)	4.69−52.79	7.466−145.582
reflns collected/unique (R_{int})	45899/5229 (0.0614)	30580/5291 (0.0772)
data/parameters	5229/358	5291/439
final R indices [$I > 2\sigma$]	R_1 = 0.0339, wR_2 = 0.0761	R_1 = 0.0688, wR_2 = 0.1876
R indices (all data)	R_1 = 0.0462, wR_2 = 0.0829	R_1 = 0.0670, wR_2 = 0.1918
GoF	1.039	1.062

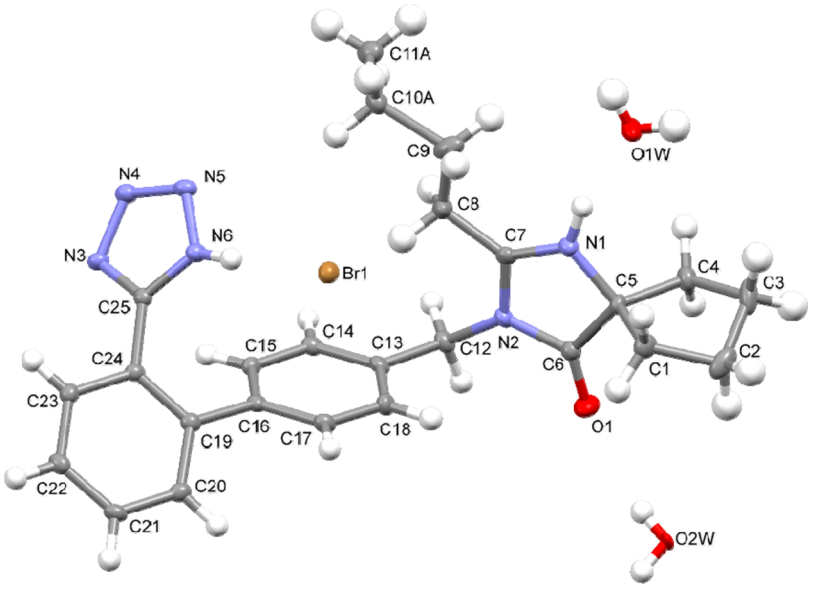

Figure 2. ORTEP view of the asymmetric unit of 1. Ellipsoid probability = 40%. For atom C10 and C11 belonging to the disordered chain just the most populated model was reported.

Geometrical calculations were performed using PARST97,[26] and molecular plots were produced using the program Mercury (v4.3.1).[27]

Crystallographic data and refinement parameters are reported in Table 1. In Figures 2 and 3, the asymmetric units of 1 and 2, respectively, are reported.

In Silico Analysis of the Crystal Structures. The crystal-packing arrangement of the two compounds was analyzed with Mercury.[27] Crystal-Explorer17[28] was used to compute the HSs and their associated 2D fingerprint plots to investigate, more in-depth, the intermolecular interactions which hold together the crystal packing of the six diastereomeric salts.

Computational Details on the Solvent Effect Study. The initial geometry of the dimeric form of IBS−DBS was extracted from the crystal structure of compound 2, which was fully optimized at the B3LYP/6-31G(d) level of theory in the gas phase and was verified to be local minima via frequency calculations. Then, the molecular geometries of the monomeric species (IBS and DBS) were isolated from the optimized dimeric form (IBS−DBS), optimized, and kept frozen to perform single-point calculations at the B3LYP/6-31G(d) in the gas phase. The interaction energy in the gas phase between the dimeric (D) and monomeric forms (M_1 and M_2) was obtained as follows

$$\Delta\Delta E_{gas} = \Delta G_{gas} D - (\Delta G_{gas} M_1 + \Delta G_{gas} M_2)$$

Single-point calculations in the gas phase and solution were performed for the optimized geometries of the compounds to estimate the free energy of solvation (ΔG_{solv}) in acetone (ACTN), ethanol (EtOH), and acetonitrile (MeCN) solvents, which were performed using Minnesota' solvation model

https://doi.org/10.1021/acsomega.2c00545
ACS Omega 2022, 7, 14897−14909

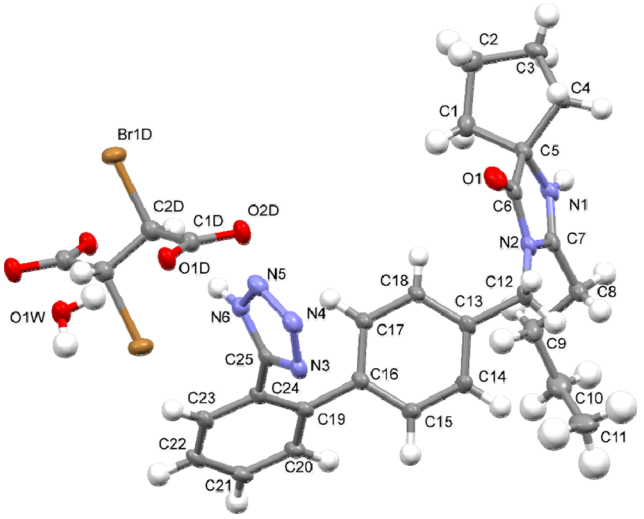

Figure 3. ORTEP view of the asymmetric unit of **2**. Ellipsoid probability = 40%.

SMD.[29] The change of solvation energy between the dimeric (D) and monomeric forms (M_1 and M_2) was computed according to the following equation

$$\Delta\Delta G_{solv} = \Delta G_{solv} D - (\Delta G_{solv} M_1 + \Delta G_{solv} M_2)$$

All calculations were performed using Gaussian 09.[30]

Powder X-ray Diffraction. PXRD patterns were recorded on a PANalytical Empyrean diffractometer equipped with a linear solid-state detector (Xcelerator). Samples were scanned with a Cu Kα source (λ = 1.5418 Å), operated at 45 kV and 40 mA, step size 0.0016°, step time 20 s, and a 2θ angular range between 4° and 50°. The powder material was placed in a zero-background sample holder measured under environmental conditions.

Fourier Transform Infrared Spectroscopy. FT-IR measurements were carried out at room temperature using a Thermo Scientific, Nicolet 6700 FT-IR equipment, fitted with a diamond attenuated total reflectance (ATR) accessory. The infrared spectrum was measured between 4000 and 400 cm^{-1} using 32 scans at 4 cm^{-1}. The samples were placed into the ATR cell without further preparation.

Solution-State NMR Studies. Solution ^1H and ^{13}C NMR analysis were performed using 10 mg of each sample and 0.5 mL of CD_3OD. Spectra were recorded on a Bruker Ascend 400 MHz instrument, and chemical shifts (δ) are reported in ppm relative to internal tetramethylsilane (δ 0.0 ppm) as standard.

Thermal Analysis. Differential scanning calorimetry (DSC) curves of the crystals produced were obtained in a DSCQ200 (TA Instrument, New Castle, DE, USA) equipped with a TA Refrigerated Cooling System 90 using aluminum crucibles with approximately 2 mg of the sample under a dynamic nitrogen atmosphere (50 mL/min) and a heating rate of 5 °C/min in the temperature range from 25 to 250 °C. The DSC cell was calibrated with a standard reference of indium. TGAs (thermogravimetric analyses) were conducted in a TGAQ500 (TA Instrument, New Castle, DE, USA). Approximately 5 mg of crystals were placed on a platinum crucible and a heating rate of 10 °C/min and temperature ranging from 25 to 800 °C using nitrogen as an inert atmosphere. The purge flow was ranged from 40 to 60 mL/min.

RESULTS AND DISCUSSION

Crystal Structures. In the asymmetric unit of **1**, one IBS cation, one bromide, and 1.5 water molecules are present, while in **2**, one molecule of protonated IBS, half 2,3 dibromosuccinate, and one water molecule are present. The conformation taken by the IBS cation in **1** well compares with that observed at room temperature in the already published structure of the bromide salt of IBS (Cambridge Structural Database, CSD,[31] Refcode NIQVIT, see Figure 4).[32] On the contrary, the conformation of IBS in **2** shows a different arrangement of the 1*H*-tetrazol-5-yl moiety (see Figure 5) due to a different value of the C15−C16−C19−C20 dihedral angle (see Table 2). In particular, (see Figure 6) if we consider the

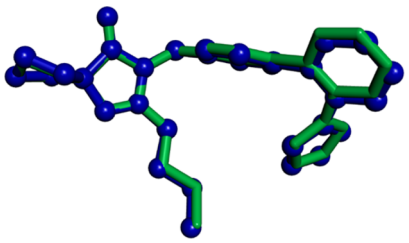

Figure 4. Superimposition of the IBS cation in **1** (blue) and NIQVIT (green).

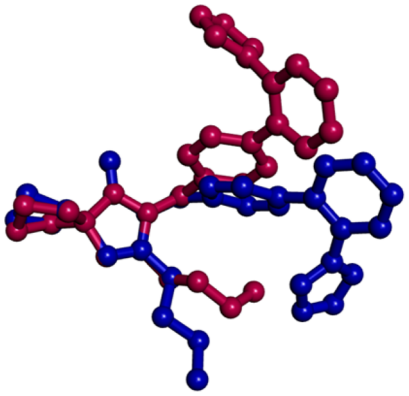

Figure 5. Superimposition of the IBS cation in **1** (blue) and **2** (pink).

Table 2. Selected Angles for 1 and 2

	1	2
N1−C7−C8−C9	−6.8(4)	−101.2(4)
C7−C8−C9−C10[a]	175.7(3)/−165.4(5)	−171.5(3)
C8−C9−C10−C11	165.1(3)/−46.1(9)	65.9(4)
N3−C25−C24−C19	127.0(3)	−63.3(4)
C15−C16−C19−C24	−44.4(3)	−46.9(4)
C6−N2−C12−C13	118.6(2)	89.5(3)
C15−C16−C19−C20	130.9(2)	−45.5(4)
C19−C24−C25−N6	−53.1(3)	118.2(3)
A/B	87.99(1)	68.1(1)
A/C	59.71(8)	71.5(1)
A/D	49.40(7)	52.2(1)
B/C	45.56(7)	46.94(8)
B/D	50.97(7)	61.9(1)
C/D	52.27(8)	64.3(1)

[a]For **1**, two values, relative to the two models, are reported.

https://doi.org/10.1021/acsomega.2c00545
ACS Omega 2022, 7, 14897−14909

mean plane defined by the carbon atoms of the C13/C18 aromatic ring in the two compounds, the 1*H*-tetrazol-5-yl moiety points in the opposite direction.

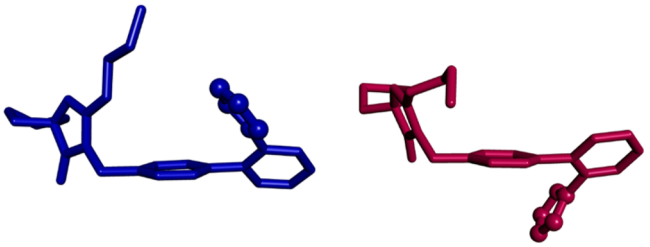

Figure 6. Relative disposition of the 1*H*-tetrazol-5-yl moiety of the IBS cation in **1** (blue) and **2** (pink).

A is the plane defined by the atoms N1, N2, C5, C6, C7; B is the plane defined by the carbon atoms of the C13/C18 ring; C is the plane defined by the carbon atoms of the C19/C24 ring and, D is the plane defined by the carbon atoms N3, N4, N5, N6, C25.

In the CSD (v. 5.42), four structures containing the IBS cation were retrieved; in addition to the already cited NIQVIT (analogous to **1** but obtained by data collected at room temperature), there is IBS hydrochloride hydrate (LIBZAY),[33] which is isomorphous and isostructural with **1**, and the salt of 6-dihydroxybenzoic acid (YUQCEV).[19] In addition, also the crystal structure of the neutral IBS (NOZWII)[17] is present in the CSD.

As evidenced in Figure 7, only in **2**, the 1*H*-tetrazol-5-yl moiety and the *n*-butyl chain point to the opposite side with respect to the C13/C18 mean plane.

Concerning the crystal packing in both the structures, a net of strong hydrogen bonds is present (see Table 3). In both cases, the IBS cation acts as a H-bond donor through the N1 and N6 nitrogen atoms, which interact with the bromide anion and the water molecule O1W in **1** and with the oxygen atoms provided by two symmetry-related 2,3-dibromo succinate anions in **2**. In addition, the IBS cation acts as an acceptor (the acceptor atoms are the N3 and O1 atoms in **1** and only the nitrogen N3 in **2**) with respect to the water molecules (O1W and O2w in **1**, O1W in **2**). All these intermolecular interactions are well evidenced in the HS of the cations, where they show up as deep red spots (Figure 8).

A visual comparison of the full and decomposed fingerprint plots of the two cations evidence that they are experiencing different chemical environments (Figures 9 and 10).

In particular, (from the upper left to the bottom right) the four spikes observed in the fingerprint plot of **1** correspond to the NH···Br^-, NH···water, N···H_2O, and C═O···H_2O, intermolecular bonds; for compound **2** the two spikes represent the NH···−OOC^- and N···H_2O intermolecular contacts. Consistently, the relative contributions to the HS area reflect these differences: H···Br 4.4%, H···O 6.0%, N···H 7.1%, O···H 3.1% for **1**; H···O 10.5%, N···H 10.5%, O···H 2.9% for **2**. Thus, as a whole, the H-bond donor contribution of the IBS cation is almost the same (10.4% in **1** vs 10.5% in **2**). The acceptor contribution, through N3 toward the crystallization water molecule, appears definitely less pronounced in **1** than in **2** (Figure 11).

Table 3. Selected H-Bonds in 1 and 2

X−H···Y	X···Y (Å)	H···Y (Å)	X−H···Y (deg)
	1		
O2W−H2WB···O1	3.006(4)	2.29(3)	166(3)
N6−H1N6···Br1	3.257(2)	2.40(3)	178(3)
N1−H1N1···O1W	2.726(3)	1.86(3)	166(3)
O1W−H1WB···N3[a]	2.887(3)	2.09(2)	166(2)
O1W−H1WB···Br1[b]	3.290(2)	2.49(3)	168(2)
O2W−H2WA···Br1[c]	3.415(3)	2.68(4)	174(5)
	2		
N6−H6N···O1D	2.652(3)	1.85(4)	168(4)
O1W−H1WB···O1D	2.888(3)	2.08(4)	160(3)
N1−H1N···O2D[b]	2.657(3)	1.87(4)	176(5)
O1W−H1WA···N3[d]	2.929(4)	2.08(4)	178(4)

[a] $x+1, y, z+1$. [b] $-x+1, -y+1, -z+1$. [c] $x, 1.5-y, 0.5+z$. [d] $-x, -y, -z$.

In **1**, a ribbon made up of two chains of IBS cations extending along the *ac* bisector originates. Within each chain, the cations are H-bonded through a water molecule (O1W) which acts both as the donor and acceptor of hydrogen bonds (see Figure 12); O1W also interacts with a bromine anion which, in turn, is H-bonded to an IBS cation belonging to the facing chain, hence the formation of a H-bonded double-chain ribbon. Adjacent ribbons are weakly bridged by the disordered water molecule O2W, which works as a bidentate donor of the H-bond toward the carbonyl oxygen atom O1 provided by the IBS cation and the bromide anions belonging to two close ribbons.

In compound **2**, each carboxylate group is H-bonded to two IBS cations and to the water molecule (see Table 3), which, in turn, further works as a donor toward a different IBS cation. The resulting network of hydrogen-bonded molecules extends in a plane parallel to the one that bisects the *ac* plane (see Figure 13). Even in this case, weak interactions are present between adjacent planes.

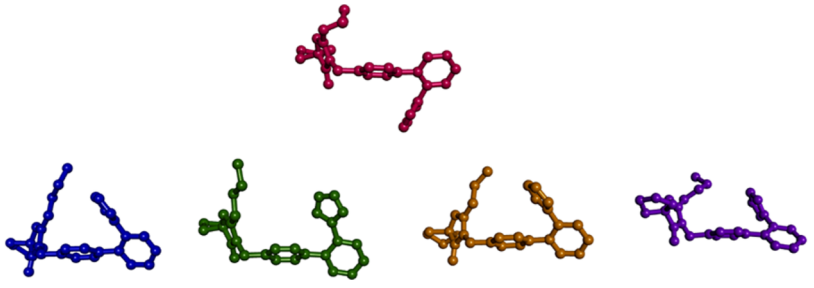

Figure 7. Relative disposition of the 1*H*-tetrazol-5-yl moiety of the IBS cation in **1** (blue), **2** (pink), NOZWII (green), LIBZAY (orange) and YUQCEV (purple).

https://doi.org/10.1021/acsomega.2c00545
ACS Omega 2022, 7, 14897−14909

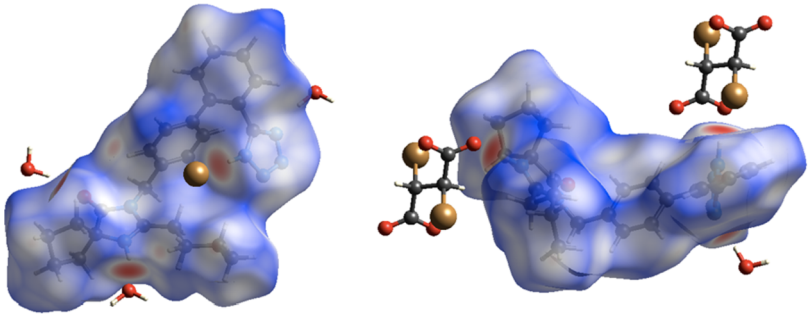

Figure 8. HSs of IBS in **1** (left) and in **2** (right) together with the closest interacting species in the crystal lattices.

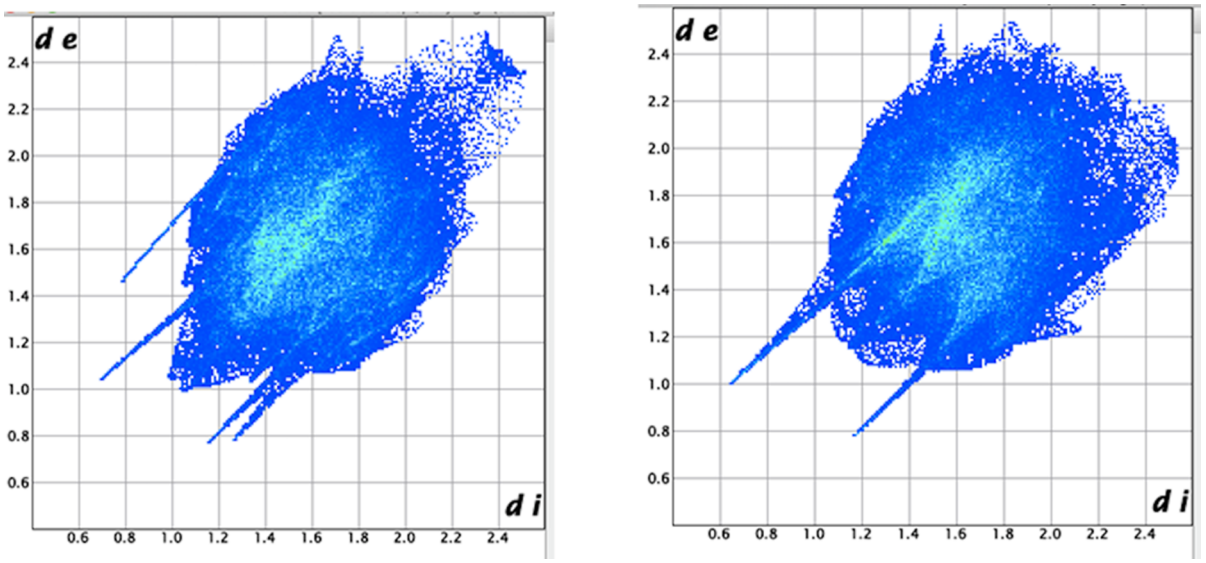

Figure 9. Full fingerprint plots of **1** (left) and **2** (right).

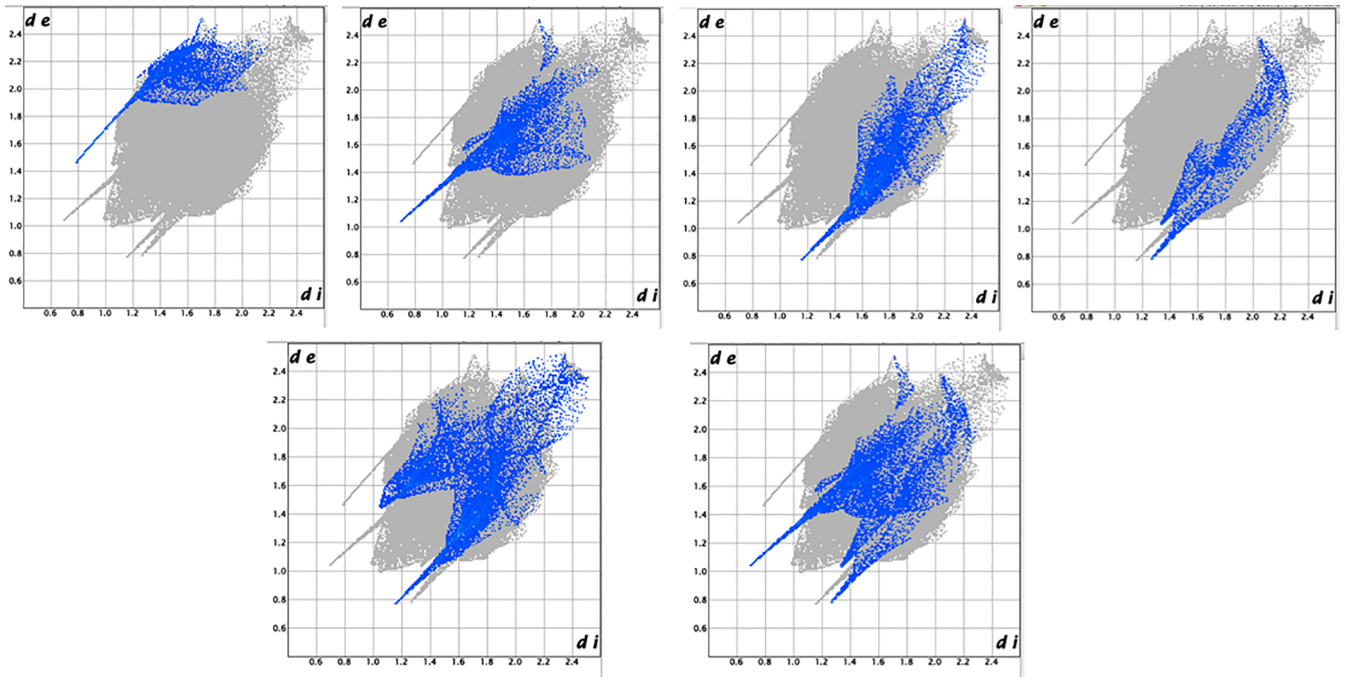

Figure 10. Decomposed fingerprint plots of **1**. Top, from left to right: H···Br, H···O, N···H, O···H. Bottom, from left to right: reciprocal N···H, O···H.

https://doi.org/10.1021/acsomega.2c00545
ACS Omega 2022, 7, 14897−14909

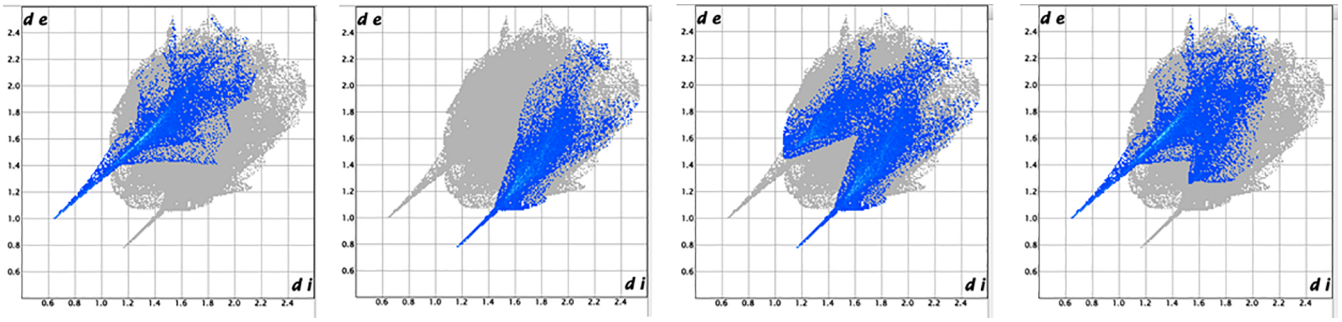

Figure 11. Decomposed fingerprint plots of **2**. Top, from left to right: H···O, N···H, reciprocal N···H, reciprocal O···H.

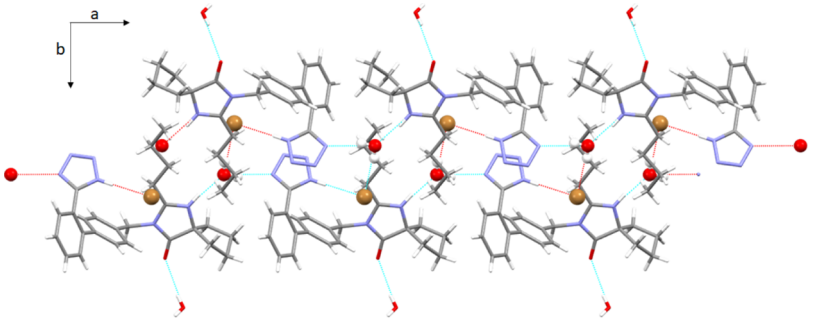

Figure 12. Hydrogen-bonded ribbon in **1**.

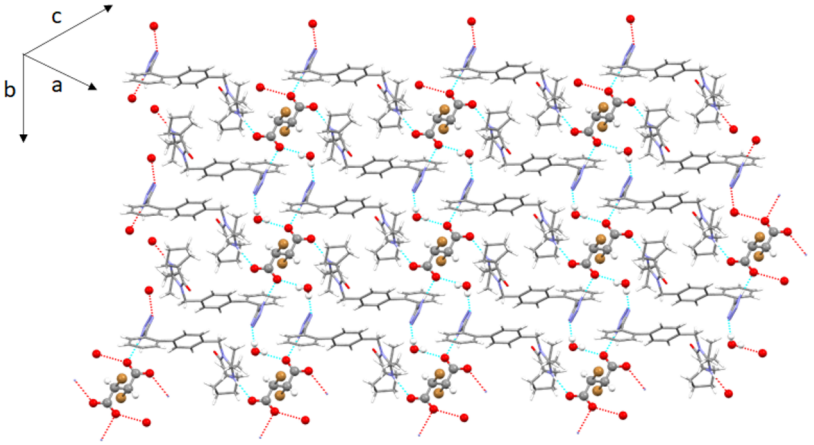

Figure 13. Hydrogen bond network in **2**.

Computational Chemistry on the Effect of Solvent. It is widely recognized that the desolvation of molecules is a dominant factor for crystal growth, where the formation of the partially desolvated molecules controls the crystallization rate,[34−36] producing unstable species able to attach spontaneously to the crystal surface.[37] We have employed quantum mechanics implicit solvation models, which have shown good predictions in cocrystal formation based on the excess enthalpy screening functions,[38] which align with the favorable interaction energy in the gas phase for the dimeric form of IBS−DBS (ca., −60 kcal/mol; see Table 4).

Since the compound **2** was only formed in EtOH, we further considered the effect of the solvent in order to predict the success in the crystal formation. The change in the solvation energy of the dimeric IBS−DBS relative to the monomeric species was computed using the SMD solvation model in ACTN, EtOH, and MeCN.

Table 4. Interaction Energy in the Gas Phase ($\Delta\Delta E_{gas}$) and the Change in the Solvation Energy (ΔG_{solv}) for the Dimeric Form of IBS−DBS in ACTN, EtOH, and MeCN

solvent	$\Delta\Delta E_{gas}$ (kcal/mol)	$\Delta\Delta G_{solv}$ (kcal/mol)
ACTN	−60.0	40.5
EtOH		43.9
MeCN		38.4

Table 4 shows that the change in solvation energy ($\Delta\Delta G_{solv}$) is less favored in EtOH considering the same dimeric form (IBS−DBS, see Figure 3) with respect to ACTN and MeCN, in agreement with the observed experimental results. Hence, the intermolecular hydrogen bond between IBS and DBS in the dimeric form shows a loss of stability with EtOH, displaying a greater value of 3.41 and 5.50 kcal/mol than ACTN and MeCN, respectively.

https://doi.org/10.1021/acsomega.2c00545
ACS Omega 2022, 7, 14897−14909

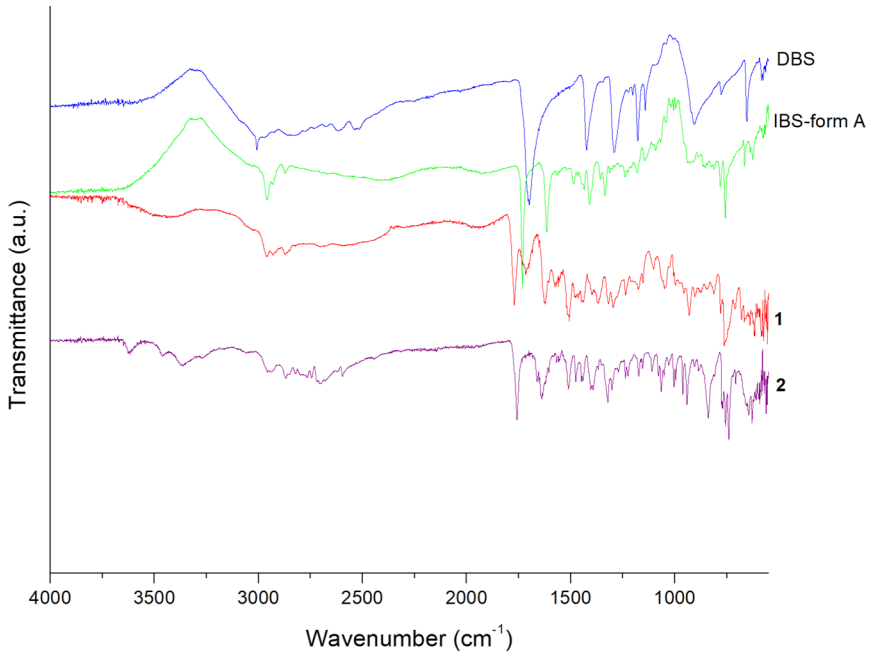

Figure 14. FT-IR spectra of DBS, IBS form A, crystals **1**, and **2**.

Table 5. ^{1}H Chemical Shifts of IBS Crystallized in EtOH, ACTN, MeCN, and Data from the Literature

	δ_H (ppm)			
position	IBS[a]	EtOH	ACTN	MeCN
1	1.82, 1.98 (m)	1.86, 1.98 (m)	2.15, 2.24 (m)	2.14−2.30 (m)
2	1.98 (m)	1.98 (m)	2.03 (m)	2.04 (m)
3	1.98 (m)	1.98 (m)	2.03 (m)	2.04 (m)
4	1.82, 1.98 (m)	1.86, 1.98 (m)	2.15, 2.24 (m)	2.14−2.30 (m)
12	4.78 (s)	4.80 (s)	5.02 (s)	5.03 (s)
14	7.16 (m)	7.17 (m)	7.30 (d, J = 8.3 Hz)	7.31 (d, J = 8.3 Hz)
15	7.16 (m)	7.14 (m)	7.20 (m)	7.20 (m)
17	7.16 (m)	7.14 (m)	7.20 (m)	7.20 (m)
18	7.16 (m)	7.17 (m)	7.30 (d, J = 8.3 Hz)	7.31 (d, J = 8.3 Hz)
20	7.69 (m)	7.67 (m)	7.71 (m)	7.71 (m)
21	7.58 (m)	7.55 (m)	7.61 (m)	7.62 (m)
22	7.69 (m)	7.55 (m)	7.61 (m)	7.71 (m)
23	7.58 (m)	7.67 (m)	7.71 (m)	7.57 (m)
8	2.40 (m)	2.47 (t, J = 7.8 Hz)	2.90 (m)	2.94 (m)
9	1.52 (m)	1.51 (m)	1.63 (m)	1.66 (m)
10	1.35 (m)	1.34 (m)	1.44 (m)	1.44 (m)
11	0.89 (t, J = 7.3 Hz)	0.87 (t, J = 7.3 Hz)	0.95 (t, J = 7.3 Hz)	0.95 (t, J = 7.3 Hz)

[a]Values published for IBS in Araya-Sibaja et al. (2019).[18]

The formation of molecular salts and cocrystals has been described to depend on the ΔpK_a values;[39] in this regard, the formation of cocrystals and molecular salts occurs when $\Delta pK_a < 1.16$ and $\Delta pK_a > 2.67$, respectively. For the molecular salt IBS−DBS reported in this study, the experimental pK_a for the hydrogen in the tetrazole ring is 7.40[40] and for DBS, 1.51 and 2.71,[41] resulting in a ΔpK_a of 4.89, which is in agreement with the reported value for molecular salts formation.

Fourier Transform Infrared Spectroscopy. The comparative FT-IR spectra of compounds **1** and **2**, as well as their individual compounds, IBS form A and DBS, are presented in Figure 14. A large number of sharp bands are observed in the spectra, which is indicative of crystalline solids' presence.[42] Furthermore, infrared spectroscopy is a quite sensitive technique for molecular interactions involving hydrogen bonding, which are common in the solid-state and present in both the compounds according to the crystal packing analysis. In FT-IR spectroscopy, hydrogen-bond formation is commonly observed as an increment in wavenumber in X−H bending.[42] In this regard, IBS presents a band at 1615 cm^{-1} related to N−H bending, which is observed at 1624 cm^{-1} and 1639 cm^{-1} in the spectrum of compounds **1** and **2**, respectively. In effect, according to the crystal structures, the IBS cation molecules interact via hydrogen bonds with the NH-containing rings (N1 and N6) in both the compounds. However, in compound **1**, the interaction occurred with bromide and a water molecule; therefore, the band related to hydrogen-bonded O−H stretching of water is observed as broadband from 3670 to 3300 cm^{-1}.[43] On the other hand, in compound **2**, the interaction occurred with the oxygen atoms

https://doi.org/10.1021/acsomega.2c00545
ACS Omega 2022, 7, 14897−14909

of the 2,3-dibromosuccinate resulting in a sharp and slightly strong band observed at 3620 cm^{-1}, corresponding with non-hydrogen-bonded O−H of water present in the structure.[43] Furthermore, DBS presents a band related to C═O stretching at 1700 cm^{-1}, characteristic of a carboxylic acid, which is observed at 1707 cm^{-1} for compound **2**, congruent with the carbonyl group in halogen-containing compounds.[43,44] This band confirms the presence of bromosuccinate in compound **2**, and its absence was corroborated by the lack of this band in compound **1**.

Solution-State NMR Studies. The results obtained with solution-state NMR support the findings on the different crystalline structures of the samples crystallized in ACTN, MeCN, and EtOH. In fact, Tables 5 and 6 summarize the data from 1-H and 13-C NMR spectra measured for IBS−DBS samples in CD_3OD, as described in the Experimental Section.

Table 6. ^{13}C NMR Chemical Shifts of IBS and Compounds Crystallized in EtOH, ACTN, MeCN, and Data from the Literature

	δ_C (ppm)			
Position	IBS[a]	EtOH	ACTN	MeCN
1	38.38	38.37	38.33	38.36
2	27.01	26.96	26.71	26.73
3	27.01	26.96	26.71	26.73
4	38.38	38.37	38.33	38.36
5	77.30	76.68	72.84	72.86
6	187.53	186.40	179.52	179.54
7	165.75	167.16	176.01	176.03
8	28.77	28.33	28.97	29.06
9	28.48	28.33	27.50	27.50
10	23.14	23.13	23.09	23.13
11	13.98	13.96	13.81	13.86
12	44.16	44.28	45.18	45.22
13	137.41	137.10	134.98	135.00
14	127.96	128.06	128.71	128.73
15	130.77	130.78	131.00	131.00
16	140.51	140.56	141.27	141.20
17	130.77	130.78	131.00	131.00
18	127.96	128.06	128.71	128.73
19	142.93	142.89	142.76	142.74
20	131.79	131.62	131.60	131.63
21	129.11	129.15	129.33	129.34
22	132.43	132.49	132.59	132.63
23	131.79	131.80	131.83	131.87
24	124.75	124.51	124.37	124.33
25	157.10	156.82	156.74	156.72

[a]Values published for IBS in Araya-Sibaja et al. (2019).[18]

As shown in Table 5, ^1H chemical shifts observed for compound **2** are analogous to data previously reported for IBS in the literature[18] for ^1H NMR measured also in CD_3OD, which is in agreement with the structure proposed for this product in the previous section. For instance, H-1 and H-4 from the cyclopentane bonded to the imidazolone ring form a multiplet at δ 1.86−1.92 ppm, while H-8 methylene forms a triplet at δ 2.80 ppm (J = 7.8 Hz) and H-12 methylene forms a singlet at δ 4.80 ppm (Figure 15), characteristic of the neutral molecule.

With respect to ^{13}C NMR, as shown in Table 6, the chemical shifts observed for compound **2** align again with the above mentioned data, previously reported in the literature,[18] which

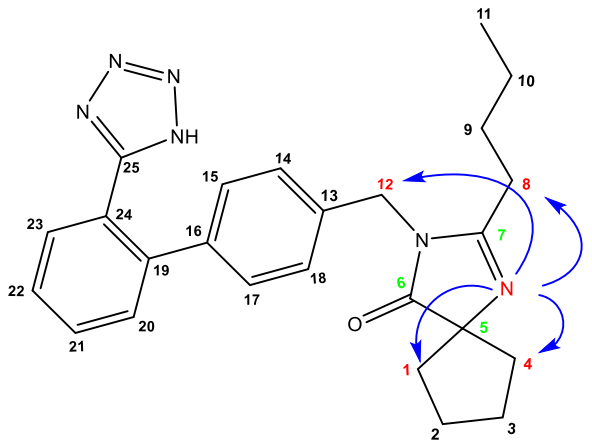

Figure 15. Differences in the ^1H and ^{13}C NMR analysis of compounds crystallized in EtOH, ACTN, and MeCN.

is also in agreement with the structure proposed in Figure 3. For instance, C-5 corresponding to the spiro bond from the imidazolone ring with the cyclopentane shows a signal at δ 76.68 ppm in agreement with being α to the carbonyl and the sp^2 nitrogen atom from the imidizolone ring. In addition, C-6 corresponding to the carbonyl shows a signal at δ 186.4 ppm, and C-7 from the imine bond shows a signal at δ 167.16 ppm, in agreement with the neutral structure.

On the other hand, the ^1H and ^{13}C NMR analysis of compounds crystallized in ACTN and MeCN show the same signal multiplicity and shifts, indicating that they correspond to the same structure in agreement with the findings of the previous sections. Furthermore, Tables 5 and 6 show that signals for compound **1** are different from the ones corresponding to compound **2**, which is again in agreement with the different structures proposed for these products (Figure 3).

In fact, regarding ^1H NMR, as shown in Table 5, signals for all protons corresponding to compound **1** have moved downfield in relation to previously reported IBS signals.[18] Furthermore, when comparing with the signals for compound **2**, the most significant changes are observed for the protons near the protonated imidazolone ring (Figure 16), supporting the structure assigned for this structure (Figure 2). For instance, as shown in the ^1H NMR spectra (Figure 16), H-1 and H-4 from the cyclopentane near the imidazolone ring show their multiplet downfield at δ 2.14−2.30 ppm, while H-8 in the aliphatic chain shows a multiplet at δ 2.94 ppm, representing a shift increase of 0.47 ppm, and H-12 singlet moved downfield at δ 5.02 ppm. These changes are in agreement with the protonation of the nitrogen in the imidazolone ring. Finally, as shown in Figure 17, the singlet at δ 4.55 ppm in compound **2** corresponds to the methine protons from the DBS, which are absent in compound **1**.

The effect of protonation on the nitrogen in the imidazolone group (Figure 2) is observed also in the ^{13}C NMR results. In fact, as shown in Table 6, all carbon signals in the samples crystallized in ACTN and MeCN have different shifts than the sample crystallized in EtOH. For instance, Figure 17 shows the ^{13}C NMR spectra with the most significant changes corresponding to the carbon atoms in the imidazolone ring. Among them, C-5 shows a signal upfield at δ 72.84 ppm, and C-6 corresponding to the carbonyl shows a signal upfield at δ 179.52 ppm, while C-7 shows a signal downfield at δ 179.52

https://doi.org/10.1021/acsomega.2c00545
ACS Omega 2022, 7, 14897−14909

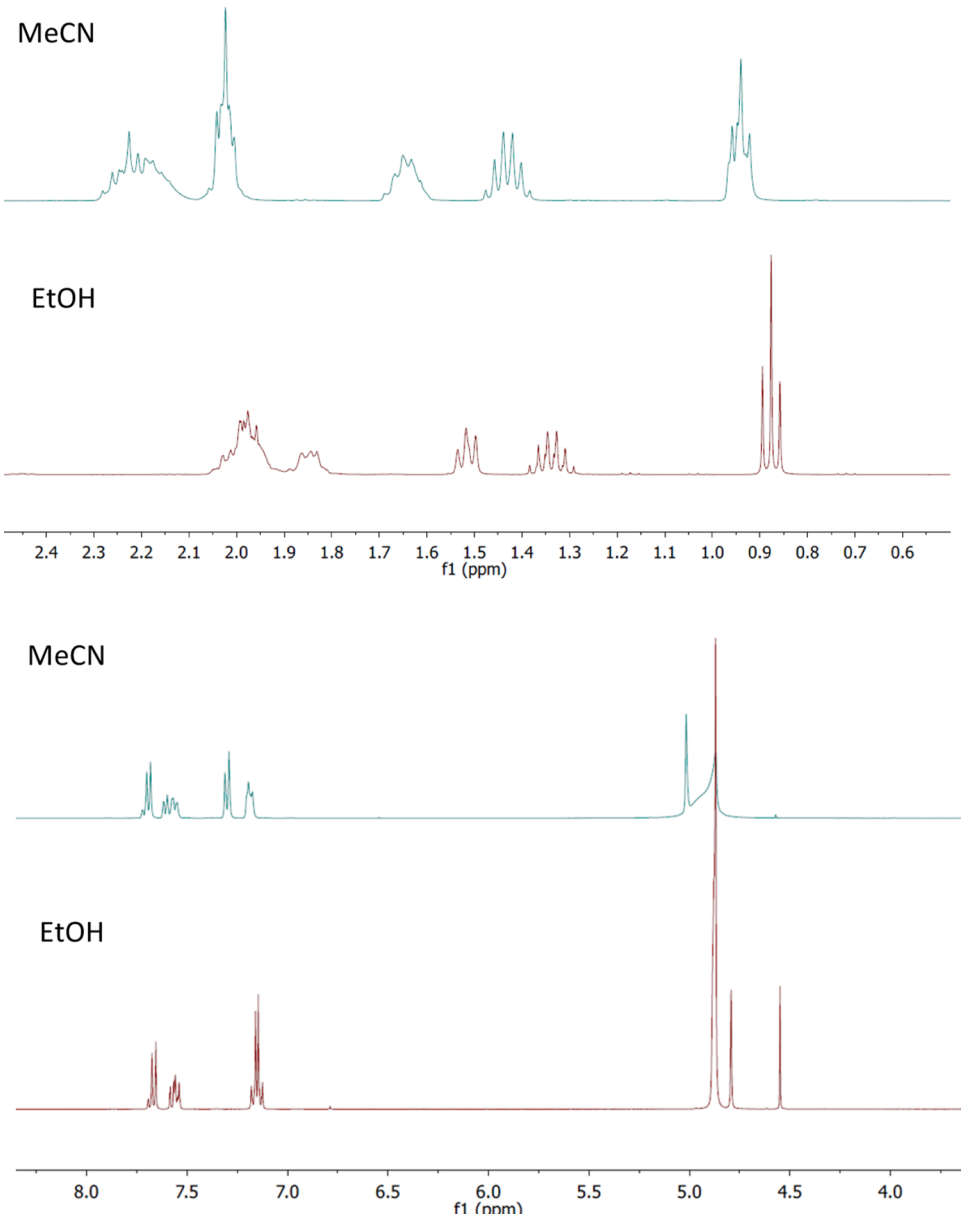

Figure 16. Characteristic signals for ^{1}H-RMN (CD_3OD) samples crystallized in MeCN and EtOH.

ppm, which aligns with previous studies in similar protonated heterocyclic rings.[45] In addition, as shown in Figure 17, the signal at δ 170.01 corresponds to the DBS carbonyl in the IBS−DBS adduct crystallized in EtOH, while this signal is absent in the IBS−DBS adduct crystallized in MeCN or ACTN. In sum, ^{1}H 13C NMR data are in agreement with the protonation of the imidazolone ring in the X-ray solid-state-assigned structure (Figure 2), which leads to a variation in the chemical shift of the surrounding atoms.

Thermal Behavior. The DSC curves of compounds **1** and **2** are presented in Figure 18a, showing an endothermic event with an onset below 100 °C, which can be attributed to water loss. In compound **1**, an exothermic event was observed around 150 °C, probably corresponding to a phase transition, and finally, a melting event was observed around 196 °C. This melting temperature was higher than those exhibited by its parent components, DBS (171.8 °C) and IBS (182.7 °C). On the other hand, compound **2** went amorphous after dehydration. Indeed, dehydration of crystalline hydrates has been considered a method for obtaining amorphous organic materials.[46]

Figure 18b shows the TGA curves of compounds **1** and **2** exhibiting different thermal decomposition behaviour. Compound **2** seems to be more stable until 300 °C.

CONCLUSIONS

Two crystal forms were obtained upon the crystallization process from IBS−DBS in EtOH, MeCN, and ACTN. The structure determination demonstrated that, in MeCN and ACTN, compound **1** crystallized in a monoclinic system $P2_1/c$, whereas in EtOH, compound **2** crystallized in a triclinic system $P\bar{1}$. For compound **2**, computational chemistry studies showed the change in solvation energy was favoured in EtOH, confirming the experimental results. In both the structures, a net of strong hydrogen bonds is present, and the FT-IR analyses confirmed their existence. In addition, the IBS cation acts as a H-bond donor through the N1 and N6 nitrogen atoms, which interact with the bromide anion and the water

https://doi.org/10.1021/acsomega.2c00545
ACS Omega 2022, 7, 14897−14909

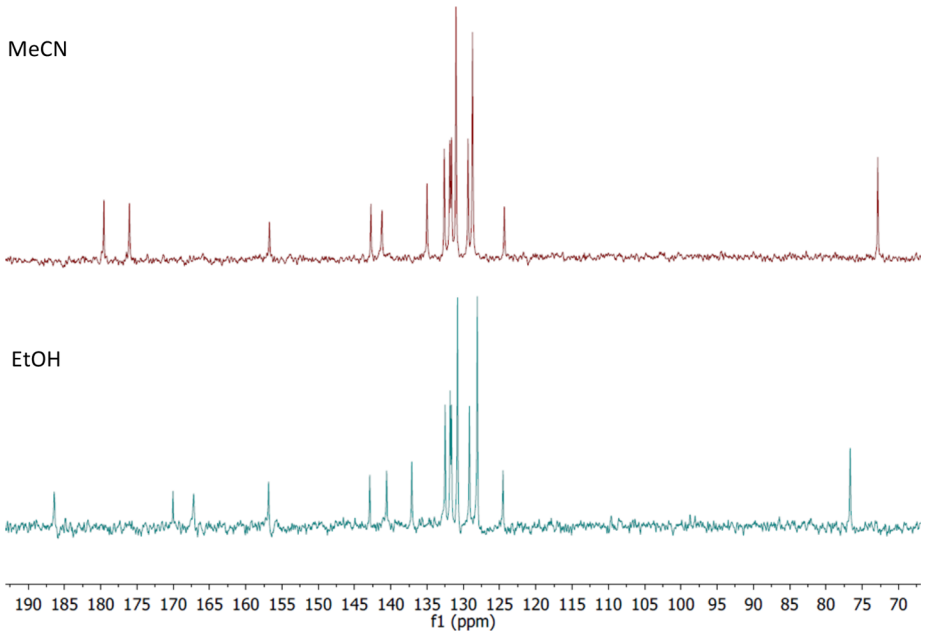

Figure 17. Characteristic signals for ^{13}C-RMN (CD_3OD) samples crystallized in MeCN and EtOH.

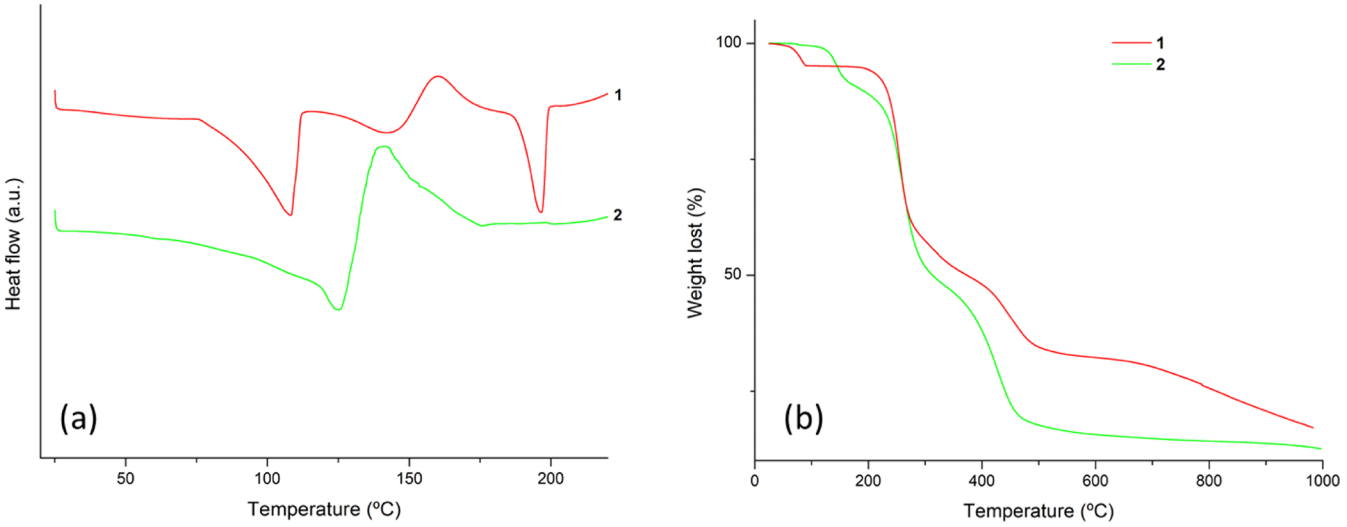

Figure 18. Thermal analysis of compounds **1** and **2**: (a) DSC curves and (b) thermograms.

molecule O1W in compound **1**. Meanwhile, N1 and N6 nitrogen atoms interact with the oxygen atoms provided by two symmetry-related 2,3-dibromo succinate anions in compound **2**. Solution-state NMR data were in agreement with the proposed protonation of the imidazolone ring in the crystal structure of compound **1**, which leads to a variation in the chemical shift of the surrounding atoms. Both the salts presented a different thermal behavior not only in melting temperature but also in thermal stability. Therefore, these results could contribute to a deeper understanding of the solvent effect in the crystallization process. In addition, these results indicate the quantum mechanics implicit solvation models as a complementary technique to support the crystallization process for this system.

AUTHOR INFORMATION

Corresponding Author

Andrea Mariela Araya-Sibaja − *Laboratorio Nacional de Nanotecnología LANOTEC-CeNAT-CONARE, 1174-1200 San José, Costa Rica;* orcid.org/0000-0001-9809-6079; Phone: +506 2519 5700 extn. 6016; Email: aaraya@cenat.ac.cr

Authors

Cinira Fandaruff − *Universidade Federal de Santa Catarina, 89040970 Florianópolis, Brazil*

Ana María Guevara-Camargo − *Laboratorio Nacional de Nanotecnología LANOTEC-CeNAT-CONARE, 1174-1200 San José, Costa Rica; Escuela de Ingeniería Química, Universidad de Costa Rica, 2060 San José, Costa Rica*

Felipe Vargas-Huertas − *Laboratorio Bioactividad para el Desarrollo Sustentable BIODESS, Escuela de Química,*

https://doi.org/10.1021/acsomega.2c00545
ACS Omega 2022, 7, 14897−14909

Universidad de Costa Rica, 2060 San José, Costa Rica; orcid.org/0000-0002-6270-0403

William J. Zamora − *Grupo CBio3, Escuela de Química, Universidad de Costa Rica, 2060 San José, Costa Rica;* orcid.org/0000-0003-4029-4528

José Roberto Vega-Baudrit − *Laboratorio Nacional de Nanotecnología LANOTEC-CeNAT-CONARE, 1174-1200 San José, Costa Rica; Laboratorio de Investigación y Tecnología de Polímeros POLIUNA, Escuela de Química, Universidad Nacional de Costa Rica, Heredia 86-3000, Costa Rica;* orcid.org/0000-0002-2002-1744

Teodolito Guillén-Girón − *Escuela de Ciencia e Ingeniería de los Materiales, Tecnológico de Costa Rica, Cartago 159-7050, Costa Rica*

Mirtha Navarro-Hoyos − *Laboratorio Bioactividad para el Desarrollo Sustentable BIODESS, Escuela de Química, Universidad de Costa Rica, 2060 San José, Costa Rica;* orcid.org/0000-0003-2115-4677

Paola Paoli − *Department of Industrial Engineering, University of Firenze, 50139 Firenze, Italy;* orcid.org/0000-0002-2408-4590

Patrizia Rossi − *Department of Industrial Engineering, University of Firenze, 50139 Firenze, Italy;* orcid.org/0000-0002-6316-338X

William Jones − *Department of Chemistry, University of Cambridge, Cambridge CB2 1EW, U.K.;* orcid.org/0000-0002-4690-4852

Complete contact information is available at: https://pubs.acs.org/10.1021/acsomega.2c00545

Notes

The authors declare no competing financial interest.

■ ACKNOWLEDGMENTS

This research was made possible by the financial support from FEES-CONARE grant number 115B5662, the University of Costa Rica (UCR) grant number 115B7202, the Costa Rica Institute of Technology (TEC), and the National Laboratory of Nanotechnology (LANOTEC). The authors thank the PINN program (PI-0132-15) of the Ministry of Science Technology and Telecommunications (MICITT) of Costa Rica and the Postgraduate Office of the TEC for the doctoral scholarships awarded to A.M.A.-S.

■ REFERENCES

(1) Rubin-Preminger, J. M.; Bernstein, J. 3-Aminobenzenesulfonic Acid: A Disappearing Polymorph. *Cryst. Growth Des.* **2005**, *5*, 1343−1349.

(2) Good, D. J.; Rodríguez-Hornedo, N. Solubility Advantage of Pharmaceutical Cocrystals. *Cryst. Growth Des.* **2009**, *9*, 2252−2264.

(3) Braga, D.; Chelazzi, L.; Grepioni, F.; Dichiarante, E.; Chierotti, M. R.; Gobetto, R. Molecular Salts of Anesthetic Lidocaine with Dicarboxylic Acids: Solid-State Properties and a Combined Structural and Spectroscopic Study. *Cryst. Growth Des.* **2013**, *13*, 2564−2572.

(4) Araya-Sibaja, A. M.; Fandaruff, C.; Wilhelm, K.; Vega-Baudrit, J. R.; Guillén-Girón, T.; Navarro-Hoyos, M. Crystal Engineering to Design of Solids: From Single to Multicomponent Organic Materials. *Mini-Rev. Org. Chem.* **2020**, *17*, 518−538.

(5) Dołęga, A.; Krupa, A.; Zieliński, P. M. Enhanced Thermal Stability of Carbamazepine Obtained by Fast Heating, Hydration and Re-Crystallization from Organic Solvent Solutions: A DSC and HPLC Study. *Thermochim. Acta* **2020**, *690*, 178691.

(6) MS, A.; Hazra, D.; Steele, G.; Pal, S. Crystallization Process Modifications to Address Polymorphic and Particle Size Challenges in Early Stage Development of an API Salt. *Chem. Eng. Res. Des.* **2020**, *164*, 400−411.

(7) Rohani, S.; Horne, S.; Murthy, K. Control of Product Quality in Batch Crystallization of Pharmaceuticals and Fine Chemicals. Part 1: Design of the Crystallization Process and the Effect of Solvent. *Org. Process Res. Dev.* **2005**, *9*, 858−872.

(8) Paul, E. L.; Tung, H.-H.; Midler, M. Organic Crystallization Processes. *Powder Technol.* **2005**, *150*, 133−143.

(9) Gao, Z.; Rohani, S.; Gong, J.; Wang, J. Recent Developments in the Crystallization Process: Toward the Pharmaceutical Industry. *Engineering* **2017**, *3*, 343−353.

(10) Rohani, S. Applications of the Crystallization Process in the Pharmaceutical Industry. *Front. Chem. Eng. China* **2010**, *4*, 2−9.

(11) Tan, J. S.; Hilden, L. R.; Merritt, J. M. Applications of In Silico Solvent Screening and an Interactive Web-Based Portal for Pharmaceutical Crystallization Process Development. *J. Pharm. Sci.* **2019**, *108*, 2621−2634.

(12) Chai, S.; Liu, Q.; Liang, X.; Guo, Y.; Zhang, S.; Xu, C.; Du, J.; Yuan, Z.; Zhang, L.; Gani, R. A Grand Product Design Model for Crystallization Solvent Design. *Comput. Chem. Eng.* **2020**, *135*, 106764.

(13) Chen, J.; Wang, J.; Ulrich, J.; Yin, Q.; Xue, L. Effect of Solvent on the Crystal Structure and Habit of Hydrocortisone. *Cryst. Growth Des.* **2008**, *8*, 1490−1494.

(14) Cui, P.; Yin, Q.; Zhang, S.; Cheng, X.; Dai, J.; Zhang, Z.; Zhou, L.; Xie, C. The Effect of Solvents on Crystal Morphology of Sucralose: Experiments and Molecular Dynamics Simulation Studies. *J. Cryst. Growth* **2020**, *532*, 125398.

(15) Salem, A.; Hagymási, A.; Vörös-Horváth, B.; Šafarik, T.; Balić, T.; Szabó, P.; Gősi, F.; Nagy, S.; Pál, S.; Kunsági-Máté, S.; Széchenyi, A. Solvent Dependent 4-Aminosalicylic Acid-Sulfamethazine Co-Crystal Polymorph Control. *Eur. J. Pharm. Sci.* **2021**, *156*, 105599.

(16) Hasa, D.; Miniussi, E.; Jones, W. Mechanochemical Synthesis of Multicomponent Crystals: One Liquid for One Polymorph? A Myth to Dispel. *Cryst. Growth Des.* **2016**, *16*, 4582−4588.

(17) Böcskei, Z.; Simon, K.; Rao, R.; Caron, A.; Rodger, C. A.; Bauer, M. Irbesartan Crystal Form B. *Acta Crystallogr., Sect. C: Cryst. Struct. Commun.* **1998**, *54*, 808−810.

(18) Araya-Sibaja, A. M.; Urgellés, M.; Vásquez-Castro, F.; Vargas-Huertas, F.; Vega-Baudrit, J. R.; Guillén-Girón, T.; Navarro-Hoyos, M.; Cuffini, S. L. The Effect of Solution Environment and the Electrostatic Factor on the Crystallisation of Desmotropes of Irbesartan. *RSC Adv.* **2019**, *9*, 5244−5250.

(19) Wang, X.; Gao, D.; Li, D.; Xie, Q.; Deng, Z.; Zhang, H. Collecting the Molecular and Ionization States of Irbesartan in the Solid State. *Cryst. Growth Des.* **2020**, *20*, 5664−5669.

(20) Araya-Sibaja, A. M.; Maduro de Campos, C. E.; Fandaruff, C.; Vega-Baudrit, J. R.; Guillén-Girón, T.; Navarro-Hoyos, M.; Cuffini, S. L. Irbesartan Desmotropes: Solid-State Characterization, Thermodynamic Study and Dissolution Properties. *J. Pharm. Anal.* **2019**, *9*, 339−346.

(21) Bruker. *Bruker APEX2*; Bruker AXS Inc.: Madison, Wisconsin, USA, 2012.

(22) Bruker. *Bruker SAINT*; Bruker AXS Inc.: Madison, Wisconsin, USA, 2012.

(23) Krause, L.; Herbst-Irmer, R.; Sheldrick, G. M.; Stalke, D. Comparison of Silver and Molybdenum Microfocus X-Ray Sources for Single-Crystal Structure Determination. *J. Appl. Crystallogr.* **2015**, *48*, 3−10.

(24) Sheldrick, G. M. A short history ofSHELX. *Acta Crystallogr., Sect. A: Found. Crystallogr.* **2008**, *64*, 112−122.

(25) Sheldrick, G. M. Crystal structure refinement withSHELXL. *Acta Crystallogr., Sect. C: Struct. Chem.* **2015**, *71*, 3−8.

(26) Nardelli, M. PARST95—an update to PARST: a system of Fortran routines for calculating molecular structure parameters from the results of crystal structure analyses. *J. Appl. Crystallogr.* **1995**, *28*, 659.

(27) Macrae, C. F.; Bruno, I. J.; Chisholm, J. A.; Edgington, P. R.; McCabe, P.; Pidcock, E.; Rodriguez-Monge, L.; Taylor, R.; van de

Streek, J.; Wood, P. A. Mercury CSD 2.0- new features for the visualization and investigation of crystal structures. *J. Appl. Crystallogr.* **2008**, *41*, 466−470.
(28) Turner, M. J.; McKinnon, J. J.; Wolff, S. K.; Grimwood, D. J.; Spackman, P. R.; Jayatilaka, D.; Spackman, M. A. *Crystal Explorer17*; University of Western Australia, 2017.
(29) Marenich, A. V.; Cramer, C. J.; Truhlar, D. G. Universal Solvation Model Based on Solute Electron Density and on a Continuum Model of the Solvent Defined by the Bulk Dielectric Constant and Atomic Surface Tensions. *J. Phys. Chem. B* **2009**, *113*, 6378−6396.
(30) Frisch, M. J.; Trucks, G. W.; Schlegel, H. B.; Scuseria, G. E.; Robb, M. A.; Cheeseman, J. R.; Scalmani, G.; Barone, V.; Mennucci, B.; Petersson, G. A.; et al. *Gaussian 09*, Revision D.01; Gaussian, Inc.: Wallingford CT, 2009.
(31) Groom, C. R.; Bruno, I. J.; Lightfoot, M. P.; Ward, S. C. The Cambridge Structural Database. *Acta Crystallogr., Sect. B: Struct. Sci., Cryst. Eng. Mater.* **2016**, *72*, 171−179.
(32) Wang, L.; Zhou, L.-N.; Bao, Y.; Wang, J.-K. 2-n-Butyl-3-[2′-(1H-tetrazol-5-yl)biphenyl-4-ylmethyl]-1-azonia-3-azaspiro[4.4]non-1-en-4-one bromide sesquihydrate. *Acta Crystallogr., Sect. E: Struct. Rep. Online* **2007**, *63*, o4933.
(33) Bartolucci, G.; Bruni, B.; Di Vaira, M.; Giannellini, V. 2-Butyl-4-oxo-3-{[2′-(1H-tetrazol-5-yl)biphenyl-4-yl]methyl}-3-aza-1-azoniaspiro[4.4]non-1-ene chloride 1.69-hydrate (irbesartan hydrochloride 1.69-hydrate). *Acta Crystallogr., Sect. E: Struct. Rep. Online* **2007**, *63*, o1529−o1531.
(34) Kowacz, M.; Putnis, C. V.; Putnis, A. The Effect of Cation:Anion Ratio in Solution on the Mechanism of Barite Growth at Constant Supersaturation: Role of the Desolvation Process on the Growth Kinetics. *Geochim. Cosmochim. Acta* **2007**, *71*, 5168−5179.
(35) Hofmann, A. E.; Bourg, I. C.; DePaolo, D. J. Ion Desolvation as a Mechanism for Kinetic Isotope Fractionation in Aqueous Systems. *Proc. Natl. Acad. Sci. U.S.A.* **2012**, *109*, 18689−18694.
(36) Piana, S.; Jones, F.; Gale, J. D. Assisted Desolvation as a Key Kinetic Step for Crystal Growth. *J. Am. Chem. Soc.* **2006**, *128*, 13568−13574.
(37) Dighe, A. V.; Singh, M. R. Solvent Fluctuations in the Solvation Shell Determine the Activation Barrier for Crystal Growth Rates. *Proc. Natl. Acad. Sci. U.S.A.* **2019**, *116*, 23954−23959.
(38) Loschen, C.; Klamt, A. Solubility Prediction, Solvate and Cocrystal Screening as Tools for Rational Crystal Engineering. *J. Pharm. Pharmacol.* **2015**, *67*, 803−811.
(39) Hill, T.; Erasmus, R. M.; Levendis, D. C.; Lemmerer, A. Combining Two Distinctive Intermolecular Forces in Designing Ternary Co-Crystals and Molecular Salts of 1,3,5-Trinitrobenzene, 9-Anthracenecarboxylic Acid and Ten Substituted Pyridines. *CrystEngComm* **2019**, *21*, 5206−5210.
(40) Jansook, P.; Muankaew, C.; Stefánsson, E.; Loftsson, T. Development of eye drops containing antihypertensive drugs: formulation of aqueous irbesartan/γCD eye drops. *Pharm. Dev. Technol.* **2015**, *20*, 626−632.
(41) Chemical Product Property chemicalbook: https://www.chemicalbook.com/ChemicalProductProperty_EN_CB9764709.htm (accessed Feb 25, 2022).
(42) Larkin, P. Environmental Dependence of Vibrational Spectra. *Infrared and Raman Spectroscopy*; Elsevier, 2011; pp 55−62.
(43) Larkin, P. J. IR and Raman Spectra-Structure Correlations. *Infrared and Raman Spectroscopy*; Elsevier, 2018; pp 85−134.
(44) Larkin, P. General Outline and Strategies for IR and Raman Spectral Interpretation. *Infrared and Raman Spectroscopy*; Elsevier, 2011; pp 117−133.
(45) Platzer, G.; Okon, M.; McIntosh, L. P. PH-Dependent Random Coil 1H, 13C, and 15N Chemical Shifts of the Ionizable Amino Acids: A Guide for Protein PK a Measurements. *J. Biomol. NMR* **2014**, *60*, 109−129.
(46) Yu, L. Amorphous Pharmaceutical Solids: Preparation, Characterization and Stabilization. *Adv. Drug Delivery Rev.* **2001**, *48*, 27−42.

https://doi.org/10.1021/acsomega.2c00545
ACS Omega 2022, 7, 14897−14909